Polymer 262 (2022) 125436

Contents lists available at ScienceDirect

Polymer

journal homepage: www.elsevier.com/locate/polymer

Charge transfer mechanisms in $40SiO_2$-$40P_2O_5$-$20ZrO_2$ /sulfonated styrene-ethylene-butylene-styrene hybrid membranes for low temperature fuel cells

B. Pascual-Jose [a], C. del Río [b], J. Mosa [c], A. Ribes-Greus [a,*]

[a] Institute of Technology of Materials (ITM), Universitat Politècnica de València (UPV), Camí de Vera, S/n, 46022, Spain
[b] Institute of Polymer Science and Technology (ICTP-CSIC), Juan de La Cierva 3, 28006, Madrid, Spain
[c] Institute of Ceramics and Glass (ICV-CSIC), Kelsen 5, 28049, Madrid, Spain

ARTICLE INFO

Keywords:
Sulfonated SEBS
Hybrid membrane
Sol-gel
Polymer electrolyte
DETA

ABSTRACT

A series of hybrid membranes synthetized via sol-gel chemistry and direct infiltration method have been prepared, consisting of sulfonated styrene-ethylene-butylene-styrene block copolymer (sSEBS), as polymeric matrix, and a zirconia modified phosphosilicate ($40SiO_2$–$40P_2O_5$–$20ZrO_2$) as inorganic component. The infiltration procedure has been carried out by immersion of sSEBS membranes in a $40SiO_2$–$40P_2O_5$–$20ZrO_2$ sol solution for 5, 10, 20, and 40 min. The hybrid infiltrated membranes (sSEBS-Zr) have been thermally characterized to further investigate their suitability as electrolytes for low temperature fuel cells. TGA thermograms showed that sSEBS-Zr were more thermally stable than sSEBS. DSC thermograms showed that the addition of inorganic component decreases the T_g of the polystyrene block in hybrid membranes sSEBS-Zr. DETA showed significant differences in the charge transfer mechanisms between low and high temperature regions. The through-plane proton conductivity analysis showed that the sSEBS-Zr infiltrated 10 min had a better proton conductive capacity at 333K, thus showing that longer infiltration times might induce excessive M-O-M′ bonds, causing competition for the available proton sites. These results indicated that the proposed methodology shows good agreement with experimental performance data in hydrogen PEMFCs. Nonetheless, when DMFCs are considered, minimizing the permeability of methanol enhances more the performance than increasing the proton conductivity.

1. Introduction

Nowadays, fuel cells are enjoying great attention for their enormous potential as emissions-free power sources [1–4]. There are several types of low temperature fuel cells but proton exchange membrane fuel cells (PEMFCs) are the most widely used for commercial applications due to the wider range of power operation and simple scaling [5]. Hydrogen is the best fuel in terms of energy conversion (chemical into electrical), but its production, storage and distribution are still severe issues to overcome. Although less reactive compared to hydrogen, methanol (CH_3OH) is considered an alternative fuel due to its high energy density and the fact that it is a liquid at atmospheric pressure and room temperature, being easier to store and distribute. Thus, direct methanol fuel cells (DMFCs) display very interesting features that make them an appropriate choice for numerous applications, such as, portable electronic devices, automobile, aviation, maritime and space applications [6]. One of the DMFC's most critical points is the methanol crossover through the polymer electrolyte. Currently, nearly all commercial DMFCs still use Nafion, even though its drawbacks related to methanol permeability are very well known [7]. The transport of methanol from anode to cathode through the membrane severely reduces the cell efficiency and makes DMFCs less competitive. For example, it has been determined that the fuel cell cost in hybrid vehicles is around 31% of its final retail price [8], from which the 38% of the overall cost is attributed to the polymer electrolyte [9].

Accordingly, in recent years there has been a necessity to develop new polymer electrolytes for DMFC that decreased the level of methanol crossover, possessed high chemical and mechanical stability, achieved good levels of proton conductivity, and were economical to produce [10,11]. Although several types of solutions are found in the literature, the study of non-fluorinated membranes has received a lot of attention due to the facility in which they can be modified [12–14]. Amidst them,

* Corresponding author.
E-mail address: aribes@ter.upv.es (A. Ribes-Greus).

https://doi.org/10.1016/j.polymer.2022.125436
Received 15 June 2022; Received in revised form 23 September 2022; Accepted 21 October 2022
Available online 23 October 2022

block copolymer ionomers are an interesting choice for fuel cell applications due to their ability to form complex segregated microstructures that, together with their high density of acid groups, favour the conduction of protons [9]. Styrene-ethylene-butylene-styrene (SEBS) block copolymer is a tough and elastic thermoplastic elastomer. Moreover, it is easy to process and has excellent thermal stability, combined with good weathering and UV resistance. Edmonson et al. [15] performed complex impedance studies on sulfonated SEBS (sSEBS) membranes and found that the obtained proton conductivity values were similar to those of Nafion 117. Moreover, at low humidity conditions, the behaviour of sSEBS was governed by a thermally activated process, thus, showing the importance of understanding the charge transfer mechanism in membranes with such a complex microstructure. Besides, Teruel-Juanes et al. [16] studied the conductivity of a set of SEBS based membranes with 10 or 25 wt% percentage of crosslinking agent divinyl-benzene (DVB) and different degrees of sulfonation. Consequently, it was found that the membranes with a lower degree of sulfonation had higher proton conductivity than those with a higher degree. Unfortunately, although a high density of sulfonic groups contributes to better proton conduction, an excessive concentration also increases the swelling, thus reducing its performance due to the lack of mechanical integrity and the high level of degradation induced in the membrane [17].

New composite materials consisting of a polymeric matrix and inorganic fillers are being studied to overcome these issues. Indeed, fillers such as silica, zirconium phosphate, titanium dioxide, montmorillonite, or single-walled carbon nanotubes are being used to obtain efficiencies closer to the pristine membranes with higher chemical, thermal and mechanical stability [13–35]. Accordingly, C. del Río et al. [36] studied a series of novel and low-cost hybrid membranes using zirconia modified phosphosilicate and sSEBS as the polymeric matrix developed via sol-gel chemistry and direct infiltration method. These hybrid membranes were previously tested in both Hydrogen and Methanol single cells showing interesting performances, finding the best results at different infiltration times depending on the fuel used [36,37]. Thus, in PEMFC the better power density was reached for the membrane infiltrated for 10 min while an infiltration time of 40 min was necessary for better results in DMFC. Such findings demonstrated the importance to establish the contribution of the proton conductive capacity against the crossover to the total power density in PEMFC or DMFC at each infiltration time. In that sense, the determination of the charge transfer mechanisms at each infiltration time and their relationship with the final power density in PEMFC or DMFC may be a useful methodology for tailoring polymer electrolytes to an optimal performance being the aim of the present work.

Thus, in order to further understand the influence of the infiltration time on thermal stability, thermal properties and proton conductivity of those hybrid membranes, thermogravimetric (TGA), calorimetric (DSC) and dielectric thermal (DETA) analysis will be related to the previous performance tests results of both hydrogen and methanol as fuels and also the charge transfer mechanisms will be determined. These properties will indicate whether these hybrid membranes are suitable in the operational range of low temperature fuel cells and are able to offer better performance than pure polymer sSEBS membranes.

2. Experimental procedure and calculations

2.1. Materials and membrane preparation

Briefly, the hybrid polymer membranes based on styrene-ethylene-butylene-styrene triblock copolymer (SEBS) were prepared from SEBS (Dynasol, Calprene CH-6120) containing 32 wt% of styrene units. The membranes were cast from chloroform solutions employing Doctor Blade technique (BYK Instruments). Regarding the sulfonation, the process was performed by immersing the membranes in a trimethylsilyl chlorosulfonate (TMSCl, Sigma-Aldrich) solution in 1,2-dichloroethane (DCE, Scharlau) with a molar concentration of 0.3 for 2 h. Concerning the infiltration process, sulfonated SEBS membranes were swelled in H_2SO_4 1 N at 353K for 2 h and then immersed in the $40SiO_2$–$40P_2O_5$–$20ZrO_2$ sol solution at 353K for 5, 10, 20, and 40 min, respectively. Then they were thermally treated to perform the inorganic polycondensation reaction at 323K for 1 h and 393K for 2 h. Finally, the membranes were cleaned with ethanol at 353K for 2 h for the last process step. Afterward, the membranes were dried for another hour at the same temperature. Fig. 1 shows both synthetic schemes of SEBS sulfonation and inorganic phase in hybrid membranes. More detailed preparation of these hybrid membranes was described elsewhere [36].

The labelling of the different hybrid membranes was performed according to the infiltration time. Consequently, the hybrid membranes are referred to as sSEBS-Zr5, sSEBS-Zr10, sSEBS-Zr20, and sSEBS-Zr40; Accordingly, neat and sulfonated polymer membranes are labelled as SEBS and sSEBS.

Table 1 compiles different physical properties of the membranes i.e., thicknesses, water uptake, dimensional changes and gain of weight according infiltration time.

2.2. Membrane characterization

2.2.1. Thermogravimetric Analysis (TGA)

The thermogravimetric analysis (TGA) was carried out with a Mettler Toledo TGA/STDA 851^e setup. The samples, with a mass between 2 and 5 mg, were placed into 70 μL alumina capsules. An empty capsule was used as a blank to take the reference baseline. The analyses were performed with a heating rate of 303 K min^{-1} over the 303K–1073K temperature range using an oxidative atmosphere with a flux of 50 mL min^{-1} of oxygen.

2.2.2. Differential Scanning Calorimetry (DSC)

The differential scanning calorimetry (DSC) analyses were evaluated using Mettler Toledo DSC822e equipment. Aluminium capsules were filled with the samples, between 2 and 4 mg, and sealed. Then, they were subjected to a heating/cooling program with a rate of 283 K min^{-1} over the 263K–473K temperature range under an inert atmosphere with the flow rate of 50 mL min^{-1} of nitrogen.

2.2.3. Dielectric Thermal Analysis (DETA)

The impedance measurements were conducted using a Novocontrol Broadband Dielectric Impedance Spectrometer (BDIS), connected to a Novocontrol Alfa-A Frequency Response Analyzer. The measurements were run in the frequency range of 10^{-1} to 10^{-7} Hz, at the temperature range of 123–473 K. The measurements were obtained under isothermal conditions by increasing in steps by 10 K.

The response to an applied electric field of a polymer consists mainly of frequency-dependent and frequency-independent components. The former is ascribed to the dc conductivity and shows a frequency-independent plateau. In contrast, the latter is attributed to the ac conductivity and is characterized by a high dispersion at higher frequencies [38]. This behaviour can be modelled by Jonscher's power law, as shown in Equation (1):

$$\sigma(\omega) = \sigma_{DC} + A\omega^n \quad \text{(Equation 1)}$$

Where A is the pre-exponential factor, σ_{DC} is the frequency-independent value, and n is the fractional exponent varying between 0 and 1.

The proton conductivity of the polymer electrolytes was calculated according to Equation (2).

$$\sigma_{prot} = {}^{L}/_{A \cdot R_0} \quad \text{(Equation 2)}$$

where R_0 refers to the protonic resistance in ohms (Ω) and is taken in the high-frequency range where the impedance tends to a non-frequency dependent asymptotic value, and the phase angle reaches its maximum [39]. L and A are geometric factors representing the thickness

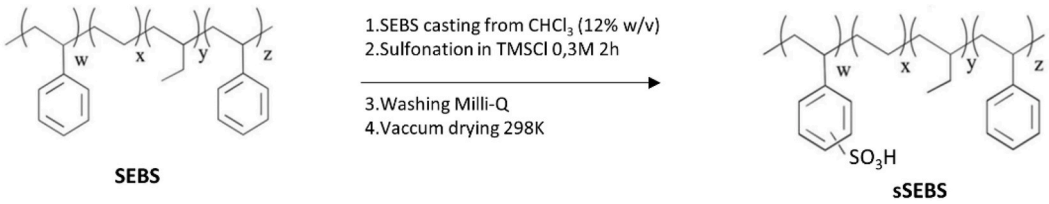

Scheme 1. Synthesis of sulfonated SEBS

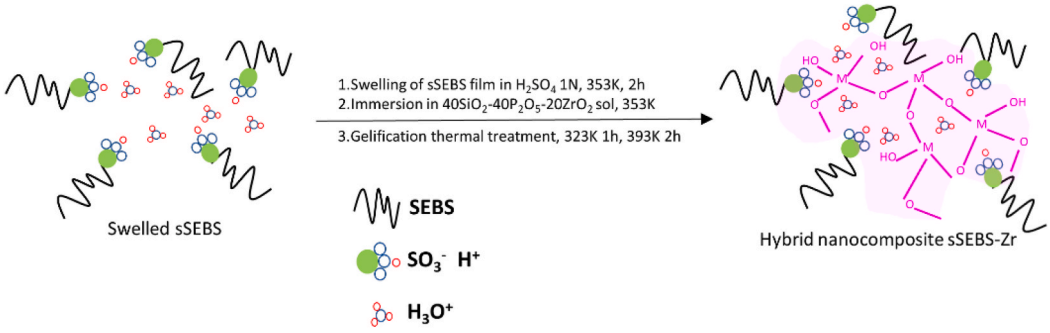

Scheme 2. Synthesis of hybrid membranes sSEBS-Zr by inorganic phase formation within sSEBS ionic phase

Fig. 1. Synthetic schemes of the (Top) sulfonated SEBS (sSEBS) and (Bottom) hybrid sulfonated SEBS (sSEBS-Zr) membranes.

Table 1
Properties of sSEBS and hybrid infiltrated membranes.

	Thickness (μm)	W_{upT} (%)	Area Increase (%)	Weight gain (%)
sSEBS	52.3	203	–	–
sSEBS-Zr5	53.0	157	117	3.2
sSEBS-Zr10	52.9	122	107	4.4
sSEBS-Zr20	55.7	105	94	4.3
sSEBS-Zr40	58.3	89	89	7.1

(cm) of the sample and the area (cm^2) of the electrode that is in contact with the membrane, respectively.

3. Results and discussion

3.1. Thermal analysis

The thermal properties of the membranes were characterized by differential scanning calorimetry (DSC). Accordingly, a controlled heating program under an inert atmosphere was carried out. The obtained thermograms, displayed in Fig. 2, show the DSC curves for 1st heating, 2nd heating, and the cooling of the neat SEBS, sulfonated sSEBS, and hybrid sulfonated sSEBS-Zr membranes in the temperature range 273–450K.

Concerning neat SEBS, there is a first endothermic peak located around 285K that is associated with the melting of the ethylene-butylene (EB) block. The second zone is located between 353K and 365K, although the largest endothermic peak is observed at 356K and is attributed to the glass transition temperature of the PS block [40].

Regarding the sSEBS, the melting temperature of the EB block is unaltered by the sulfonation process. The temperature of the prominent endothermic peak increases up to 388K, and the glass transition increases due to steric hindrance effects generated by the sulfonation process. However, this prominent endothermic peak represents two different processes that are overlapped. More specifically, these two processes are the glass transition and the elimination of the clusters located in the sulfonated PS domains. It is noteworthy to mention that the inorganic component has been found to be directed towards these ionic domains, which might result in an increment of the clusters' size. Furthermore, these clusters disappear during the first heating and cannot be traced in the second heating. Accordingly, no predominant peak is found in SEBS since there cannot be a cluster formation phase, as observed in other works [41,42].

Concerning the hybrid sulfonated membranes, all the samples display the same two endothermic peaks regardless of the infiltration time. The endothermic peak associated with the glass transition of the PS block is mostly unaltered. Only the sSEBS-Zr10 displays a lower value (383K). According to some references, the addition of inorganic fillers related to the infiltration time, can be responsible for lowering the glass transition temperature [43,44].

The thermal stability of sSEBS and hybrid sSEBS-Zr membranes was assessed through thermogravimetric analysis (TGA). The samples were subjected to a dynamic thermal program under an oxidative atmosphere. The weight loss as a function of time is shown in (Fig. 2A) and differential curves appear in Fig. 2B. Three different stages are observed, the first stage occurs between 333K and 523K, and it is related to the loss of residual water. Moreover, a second stage is observed between 523K and 698K that is related to the desulfonation process and loss of aromatic rings of the polystyrene blocks. The third stage at temperatures above 698K up to 794K is linked with the thermal degradation of the main polymer chain [40,42,45,46].

In Fig. 3A, the thermogravimetric curves for all hybrid sSEBS-Zr are also displayed. These membranes present a multiple-stage degradation. As in the case of sSEBS, the first stage is attributed to the release of water molecules. Accordingly, hybrid membranes with high infiltration times, such as sSEBS-Zr20 and sSEBS-Zr40, display a lower mass percentage than the sSEBS membranes at a similar temperature range. The second

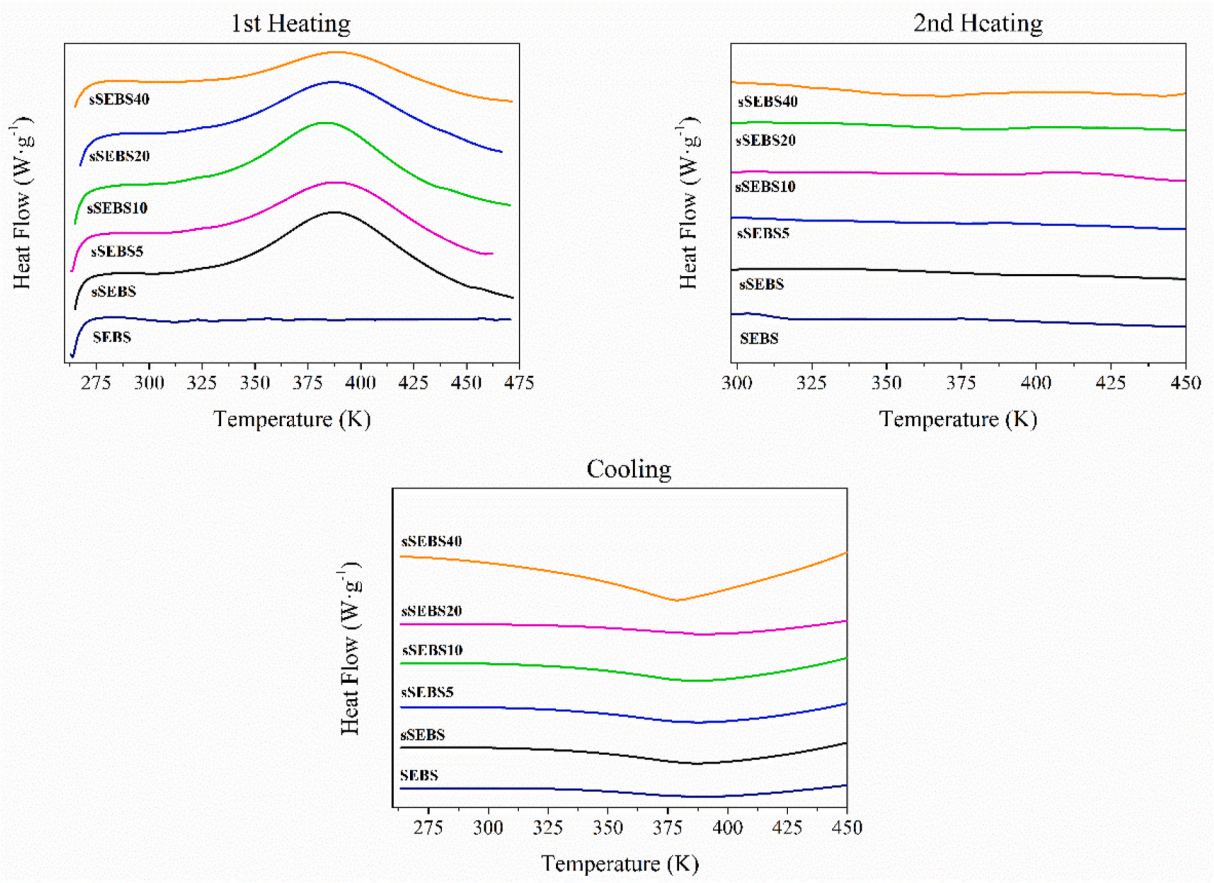

Fig. 2. DSC thermograms of the neat (SEBS), sulfonated SEBS (sSEBS) and hybrid sulfonated SEBS (sSEBS-Zr5, sSEBS-Zr10, sSEBS-Zr20 and sSEBS-Zr40) membranes.

stage is associated with the decomposing of the sulfonic acid groups and again, these hybrid membranes are more thermally stable than sSEBS as the peak temperature (in the derivative curve) increases to 625K. The third stage is attributed to the thermal degradation of the aromatic rings of the polystyrene blocks, and for the sSEBS membrane, this process occurs between 523K and 723K. The addition of the inorganic component ($40SiO_2$–$40P_2O_5$–$20ZrO_2$), related to the infiltration time, shifts a bit the peak temperature of the process, but no significant differences are found. The same conclusion is reached in the last stage, occurring at temperatures higher than 773K, attributed to the backbone degradation [17].

In general, it is observed that the addition of the inorganic component has an increment in the thermal stability of these membranes. Accordingly, Mistry et al. [42], which analysed a series of hybrid membranes formed with sSEBS as matrix and silica as the inorganic filler, found that all hybrid membranes displayed enhanced thermal stability compared with sSEBS. Indeed, the onset of the thermal decomposition was found to increase between 313K and 363K. Accordingly, the results presented in Fig. 3 show the same tendency. As the infiltration times increase, and therefore more extensive inorganic network is grown across the membrane, the thermal stability increases.

3.2. Electric conductivity

The dielectric conductivity of the SEBS, sSEBS, and hybrid sSEBS-Zr membranes have been analysed in the frequency range 10^{-1} to 10^{7} Hz between 123K and 473K in steps of 10K. The loss permittivity of the sSEBS-Zr10 is displayed in Fig. 4 to illustrate the different molecular motions that take place in all the studied membranes since the analysis of the electric conductivity cannot be performed without considering the molecular processes present in all the membranes.

In this regard, the dielectric spectra of the neat SEBS, sSEBS, and hybrid sSEBS-Zr consist of three molecular processes: a low-temperature β relaxation and the glass transition of each of the two blocks ethylene-butylene (α_{EB}) and styrene (α_{PS}), respectively [47]. Any variation in these molecular processes must be considered since they can significantly modify the mechanisms giving rise to the electric conductivity.

In Fig. 5, the isothermal curves of the module of the complex conductivity for the complete temperature range are displayed. The permittivity curves show that the dielectric relaxations at higher temperature are coupled with ion transfer. The molecular motions, which are the origin of both glass transitions (α_{EB}, α_{PS}), play an important part in the ion transfer due to their inherited cooperative nature. However, the curves plot in Fig. 5 indicate that the β relaxation that occurs at very low temperatures has few effect on the conductivity, although some works have found high levels of electric conductivity in the glassy state of some amorphous polymers. The sudden decrease in conductivity after the dc plateau is reached signals the onset of electron polarization. As the temperature decreases, this phenomenon is shifted towards lower frequencies as the overall dynamics slow down, and therefore, it is out of range [48–50].

Regarding the sSEBS-Zr hybrid membranes, significant variations are found compared to the sSEBS and, as the infiltration time increases, the spectra tend to match that of neat SEBS. This result is in line with other studies with hybrid membranes [26] and it can be explained by the wide spreading of the inorganic component across the entire membrane thickness. In this sense, Escribano et al. [36] found by EDX cross-section analysis that the concentration of the inorganic elements increased as a function of infiltration time, filling the entire thickness of the membrane in the case of sSEBS-Zr40. The inorganic component ($40SiO_2$–$40P_2O_5$–$20ZrO_2$) appears well distributed over the entire depth of the membrane at longer times, resulting in a barrier that acts as an

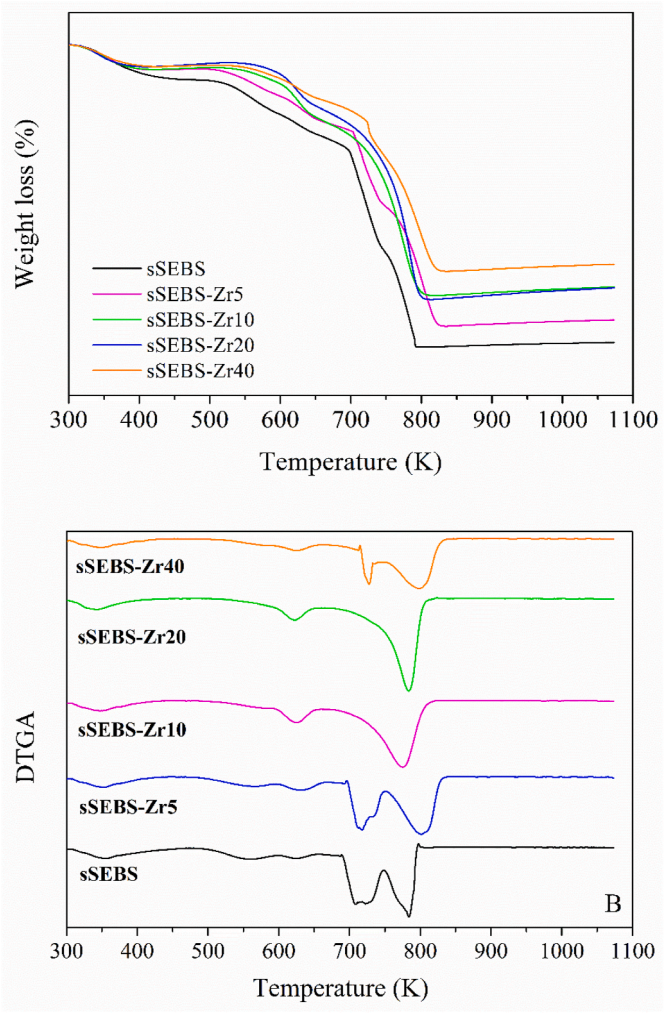

Fig. 3. Thermogravimetric curves of sSEBS and all hybrid SEBS (sSEBS-Zr5, sSEBS-Zr10, sSEBS-Zr20, and sSEBS-Zr40) membranes.

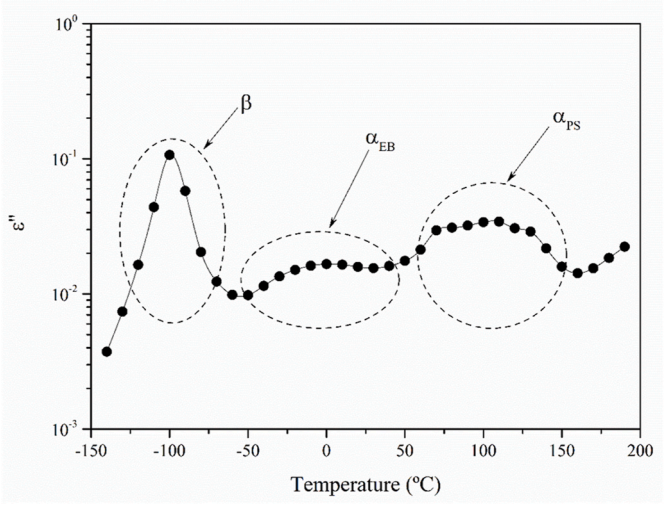

Fig. 4. The isochronal curve of the loss permittivity for the sSEBS-Zr10 at 1 kHz.

insulating layer. Subsequently, a significant decrease in conductivity is produced, as shown by sSEBS-Zr40 compared to the other hybrid membranes, except for the spectra of sSEBS-Zr5, which is quite similar to that of sSEBS since the filler's concentration is still low at that stage.

To assess the conductivity, Jonscher's power law is used [38,51]. Subsequently, the real part of the complex conductivity can be approximated as described in Eq. (1). The best fits for all the membranes at a temperature of 363K are displayed in Fig. 6, and the values of the Jonscher's parameters at several temperatures are gathered in Table 2.

The conductivity curves shown in Fig. 6 display different transition zones related to the molecular relaxation processes. The values of σ_{DC} rise with increasing temperature, which is a sign of a thermally activated process. There are important differences in the values found for sSEBS and the hybrids sSEBS-Zr. At lower temperatures, the values are higher for sSEBS-Zr5 than for sSEBS but they continue decreasing with increasing infiltration time, especially for sSEBS-Zr40. Additionally, the exponent n can also provide useful insights since it is understood as a qualitative index of the morphological texture. Subsequently, values closer to 1 refer to ideal systems with good long-range pathways between the ionic clusters, whereas values lower than 0.5 account for an ion conductive network with high levels of tortuosity [52]. All the membranes display values larger than 0.7, and no significant differences among them are found, meaning that the addition of the inorganic component ($40SiO_2$–$40P_2O_5$–$20ZrO_2$) is not affecting the morphological texture of the ionic pathways. Therefore, all hybrid membranes sSEBS-Zr maintain the same microstructure of the sSEBS membrane, which agrees with previous results [36].

To provide further insights into the nature of the charge transport process and how it varies with the addition of the inorganic component ($40SiO_2$–$40P_2O_5$–$20ZrO_2$), it is necessary to estimate the temperature dependence of the dc conductivity.

In Fig. 7, the Arrhenius plot for the σ_{DC} of all the copolymers is displayed. All membranes are in the glassy state in the low-temperature region (Zone I), where only local motions are active. The temperature dependence of the conductivity is constant, and very few differences between the membranes are found. In this state, where no cooperative motions are possible, the ion transfer is completely decoupled from the molecular relaxations. Nonetheless, polymers still have decent levels of conductivity [48]. Polymers in the glassy state are found to have ion transferring in a partially diffusive mode [49]. Thus, in this landscape, the main factor ruling the rate of ion hopping is the activation energy (E_a) [50].

In the mid-temperature region (Zone II), notable differences among the membranes are found. Accordingly, the SEBS membrane displays the lowest values of dc conductivity, with a nearly constant variation against temperature that reflects its nonpolar behaviour. On the contrary, sSEBS displays the highest values of dc conductivity thanks to the inclusion of the sulfonic groups. There is a change in the ion transfer mechanism since its temperature dependence is described by a VFTH-like behaviour, meaning that the ion transfer is coupled with molecular relaxation. The same behaviour is found in sSEBS-Zr10 and sSEBS-Zr20 membranes. On the contrary, for the lowest and highest times, 5 or 40 min of the infiltration process respectively, its thermal dependence is described by an Arrhenius-like behaviour. Hence, the ion transferring is decoupled from the molecular motion.

The reasons behind this change differ between membranes. In the case of the sSEBS-Zr5, ionic conductions always follow the path of least resistant, i.e., the lower energy barrier (E_a). These charges at the surface contribute to reducing the energy barrier and, therefore, explain the decoupling from the relaxation process, as already observed in other polymers [49,50]. Regarding the sSEBS-Zr40, the high concentration of inorganic component ($40SiO_2$–$40P_2O_5$–$20ZrO_2$) implies that the surface is completely coated [36], which acts as an electric insulator.

Another significant difference is the shape of the curves. Both neat SEBS and sulfonated sSEBS are continuous, and the transition between both temperature regions is seamless. On the contrary, the hybrid membranes present a clear gap between molecular processes that seem to accentuate as the inorganic component ($40SiO_2$–$40P_2O_5$–$20ZrO_2$) increases. Consequently, as the concentration increases, it spreads

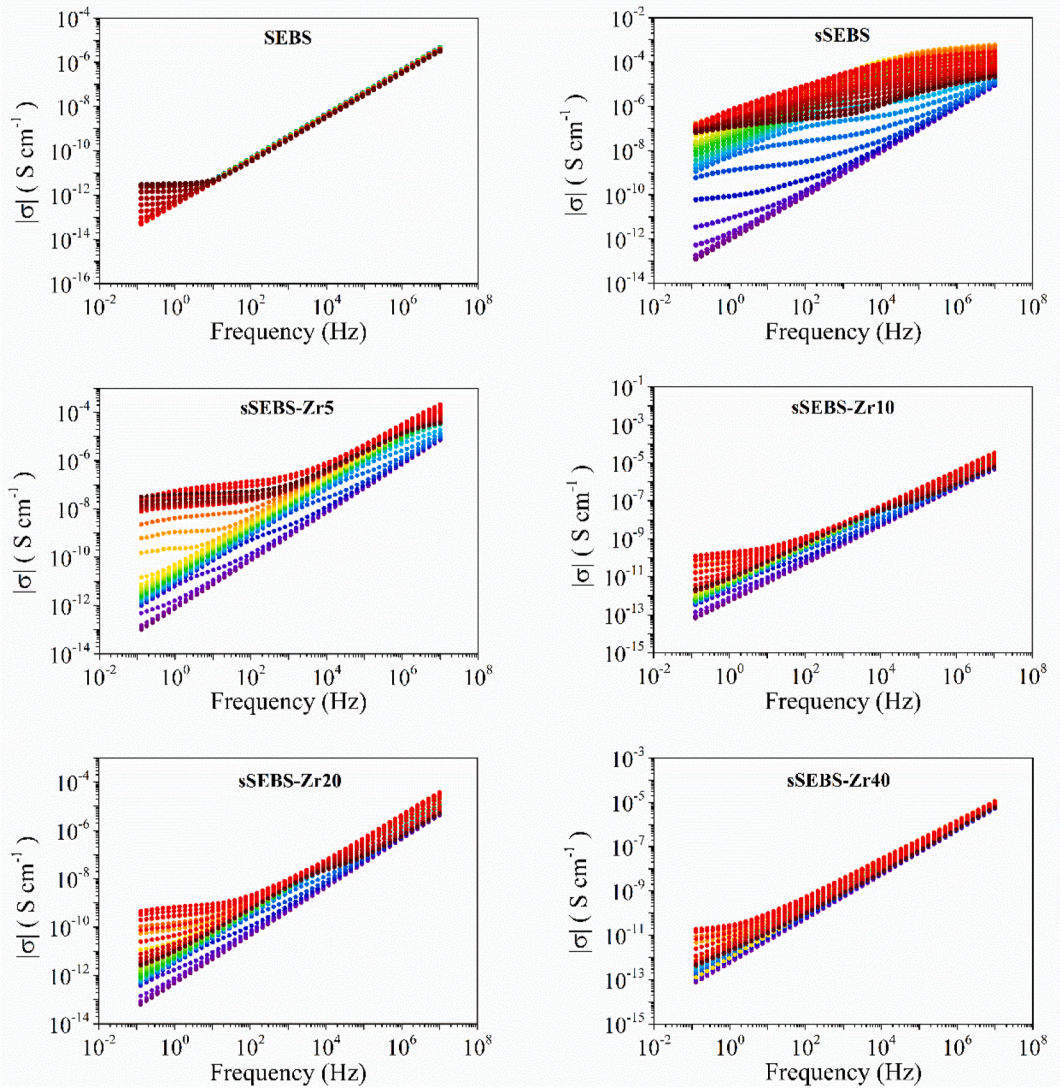

Fig. 5. Isothermal curves of the module of the complex conductivity (σ*) for the styrene-ethylene-butylene-styrene (SEBS), sulfonated SEBS (sSEBS) and all hybrid SEBS (sSEBS-Zr5, sSEBS-Zr10, sSEBS-Zr20 and sSEBS-Zr40).

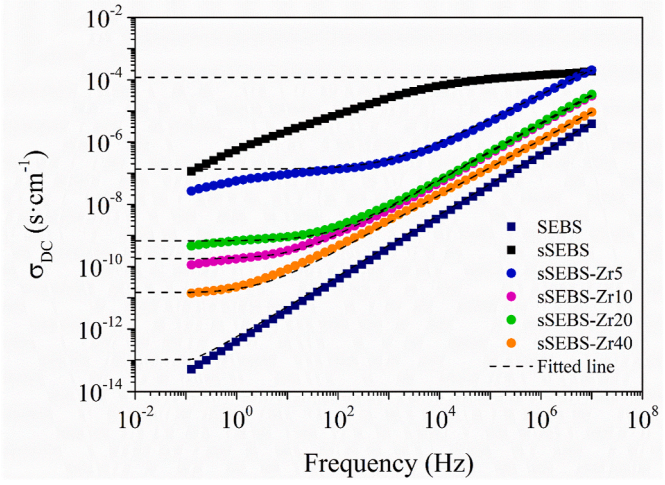

Fig. 6. Isothermal curves of the real part of the electric conductivity (σ_{DC}) for all hybrid sSEBS-Zr (sSEBS-Zr5, sSEBS-Zr10, sSEBS-Zr20, sSEBS-Zr40) at a temperature of 363 K. The dashed lines represent the fit through the Jonscher's power law.

evenly across the entire depth of the membranes, and a stronger oxygen network (M-O-M′ bonds, being M = Si, P, or Zr) delays the activation of the molecular processes.

In the high-temperature region (Zone III), it is interesting to observe that all the membranes display the same charge carrier mechanism. At these temperatures, cooperative motions are easily activated, and therefore the relaxation process (α_{PS}) is coupled with the ion transferring. This is clear evidence that this set of membranes maintains a good performance at high temperatures. Nonetheless, the peak occurs at an intermediate temperature among sulfonated sSEBS and neat SEBS. This result agrees with the DSC data, and it could be ascribed to the plasticization process induced by the addition of the inorganic component ($40SiO_2$–$40P_2O_5$–$20ZrO_2$). On the other hand, the maximum peak temperature of sSEBS-Zr is lower than SEBS because of the latter's nonpolar nature, which greatly difficulties the activation of the charge carrier mechanisms.

The apparent activation energy (E_a) values are gathered in Table 3. The sSEBS membrane requires around 67 kJ mol^{-1} to activate the dc conductivity in temperature zone II while only around 38 kJ mol^{-1} to initiate the one regarding temperature zone III. Once the chain begins its motion, it takes less energy to initiate the motion at high temperatures. Thus, it shows the importance of molecular motions' coupling/decoupling behaviour. Only sSEBS-Zr10 and sSEBS-Zr20 follow this tendency

Table 2
Jonscher's parameters of the sulfonated and hybrid sSEBS-Zr membranes.

	T (K)	σ_{DC} x 10^{13} (S·cm^{-1})	A · 10^{13}	n	R^2
sSEBS	163.15	3.53×10^{1}	1.86×10^{0}	0.987	0.999
	183.15	3.27×10^{4}	4.56×10^{0}	0.943	0.999
	313.15	2.43×10^{9}	6.86×10^{5}	0.858	0.847
	363.15	6.15×10^{8}	5.50×10^{6}	0.825	0.998
	413.15	8.06×10^{7}	1.79×10^{6}	0.826	0.973
sSEBS-Zr5	163.15	2.48×10^{2}	1.97×10^{0}	0.974	0.999
	183.15	2.66×10^{5}	4.35×10^{0}	0.937	0.999
	313.15	2.32×10^{3}	7.19×10^{1}	0.933	0.999
	363.15	1.37×10^{6}	1.34×10^{3}	0.794	0.999
	413.15	2.43×10^{5}	2.93×10^{2}	0.828	0.985
sSEBS-Zr10	163.15	1.26×10^{1}	1.34×10^{0}	0.972	0.999
	183.15	6.91×10^{3}	2.04×10^{0}	0.953	0.999
	313.15	1.22×10^{2}	1.60×10^{1}	0.937	0.999
	373.15	1.78×10^{3}	2.79×10^{1}	0.902	0.999
	413.15	2.87×10^{6}	1.61×10^{1}	0.854	0.974
sSEBS-Zr20	163.15	1.10×10^{1}	1.25×10^{0}	0.971	0.999
	183.15	5.54×10^{3}	1.99×10^{0}	0.950	0.999
	313.15	3.50×10^{2}	1.95×10^{1}	0.934	0.999
	373.15	6.72×10^{3}	2.74×10^{1}	0.909	0.999
	413.15	3.42×10^{6}	1.73×10^{1}	0.843	0.956
sSEBS-Zr40	163.15	1.06×10^{0}	1.31×10^{0}	0.976	0.999
	183.15	1.75×10^{0}	1.53×10^{0}	0.969	0.999
	313.15	2.61×10^{1}	1.46×10^{1}	0.881	0.999
	373.15	1.42×10^{2}	1.06×10^{1}	0.890	0.999
	413.15	5.79×10^{0}	1.84×10^{0}	0.966	0.999

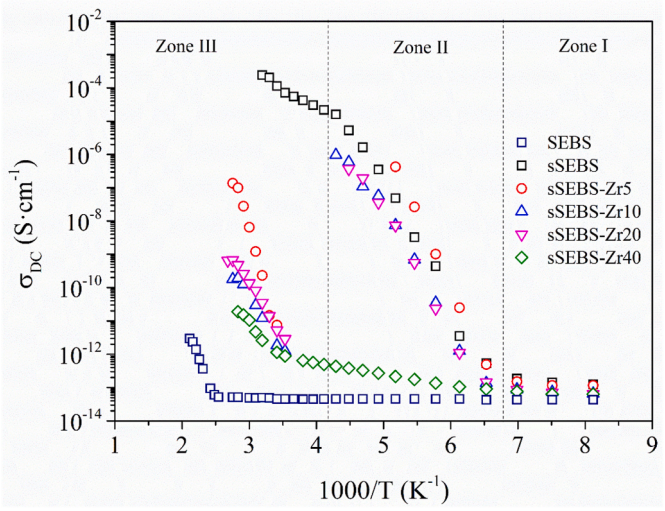

Fig. 7. Arrhenius plot of the DC conductivity (σ_{DC}) for the sulfonated SEBS (sSEBS) and all hybrid SEBS (sSEBS-Zr5, sSEBS-Zr10, sSEBS-Zr20 and sSEBS-Zr40).

Table 3
The activation energy (E_a) for the σ_{DC} of the sSEBS and sSEBS-Zr membranes.

	Sample	E_a (kJ·mol^{-1})	R^2
Temperature Zone II	sSEBS	67	0.987
	sSEBS-Zr5	85	0.999
	sSEBS-Zr10	62	0.985
	sSEBS-Zr20	64	0.988
	sSEBS-Zr40	62	0.995
Temperature Zone III	sSEBS	38	0.985
	sSEBS-Zr5	144	0.986
	sSEBS-Zr10	71	0.999
	sSEBS-Zr20	58	0.982
	sSEBS-Zr40	45	0.964

with very similar values for both membranes. Thus, it takes the same energy to activate both conductive processes.

On the contrary, sSEBS-Zr5 has large values for both activation energies, although it is larger for Zone III. Thus, there is a big gap between them. Moreover, sSEBS-Zr40 seems to be very easy to initiate the motion of the ions at low temperatures, and it takes more effort (large energy barrier) to generate the motion of ions at high temperatures. Indeed, the largest differences are established for the materials that transition from the decoupled to the coupled behaviour.

The proton conductivity at 333 K and dry conditions is determined as stated in Equation (2), and the results are plotted in Fig. 8. In addition, it clearly shows that different criteria must be held to apply the proposed methodology to determine whether a specific polymer is suitable for DMFC applications. Regarding PEMFCs, a comprehensive analysis of the molecular mobility and the charge transfer mechanisms is shown to provide consistent data on the performance of a polymer as an electrolyte in a PEMFC. In such cases, having a microstructure that favours proton exchange through high levels of molecular mobility is the most paramount criterion. Indeed, the results indicate that the sSEBS-Zr10 is the best performer at 333K. This criterion is validated by the results presented in a previous work, which showed the same tendency for power density curves analysed at 333K, but in a hydrated state (Fig. 9). Briefly, performance tests were carried out using a Scribner 850e multi range fuel cell test system using hydrogen as fuel and oxygen as oxidant (200 mL min^{-1}), at atmospheric pressure, 333 K cell temperature and 100% relative humidity for PEMFC. Regarding DMFC, the polarization curve measurements were conducted at 333 K supplying 1 M methanol solution at 3 mL min^{-1} and pure humidified oxygen at 100 mL min^{-1} and 1 bar to anode and cathode, respectively. More information about the electrochemical characterization of membrane-electrodes assemblies can be found elsewhere [36,37]. Consequently, the two membranes with better performance are the ones where the ion diffusivity maintains their coupling with the molecular processes. Thus, it is clear that excessive addition of the inorganic component ($40SiO_2$–$40P_2O_5$–$20ZrO_2$) will induce an excessive amount of M-O-M′ bonds, causing a blocking effect for proton transport.

The coupling or decoupling from the molecular motions in the charge transfer mechanisms plays an important role, which is decisive in the behaviour of these membranes when used as electrolytes in hydrogen PEMFC. Nevertheless, this does not occur when these membranes act as electrolytes in DMFC. Fig. 9 also displays the maximum power density values obtained when these hybrid membranes are used as electrolytes in a DMFC [37]. A quick comparison with other published data shows that the maximum power density values offered by sSEBS-Zr10 for PEMFCs and sSEBS-Zr40 for DMFCs are in line with the

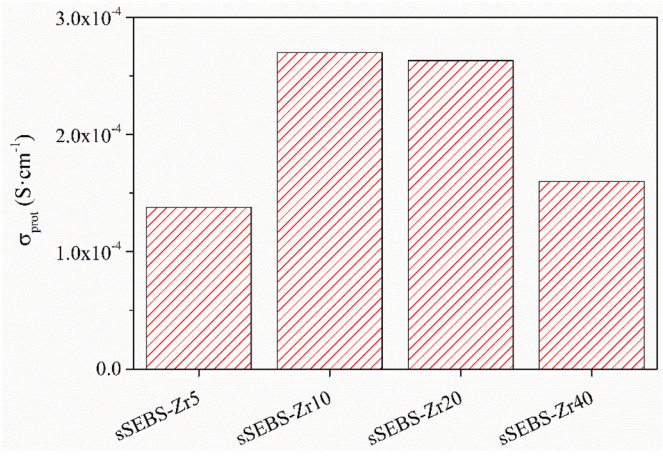

Fig. 8. Through-plane protonic conductivity (dry) at 333K for the hybrid sSEBS-Zr (sSEBS-Zr5, sSEBS-Zr10, sSEBS-Zr20 and sSEBS-Zr40) membranes.

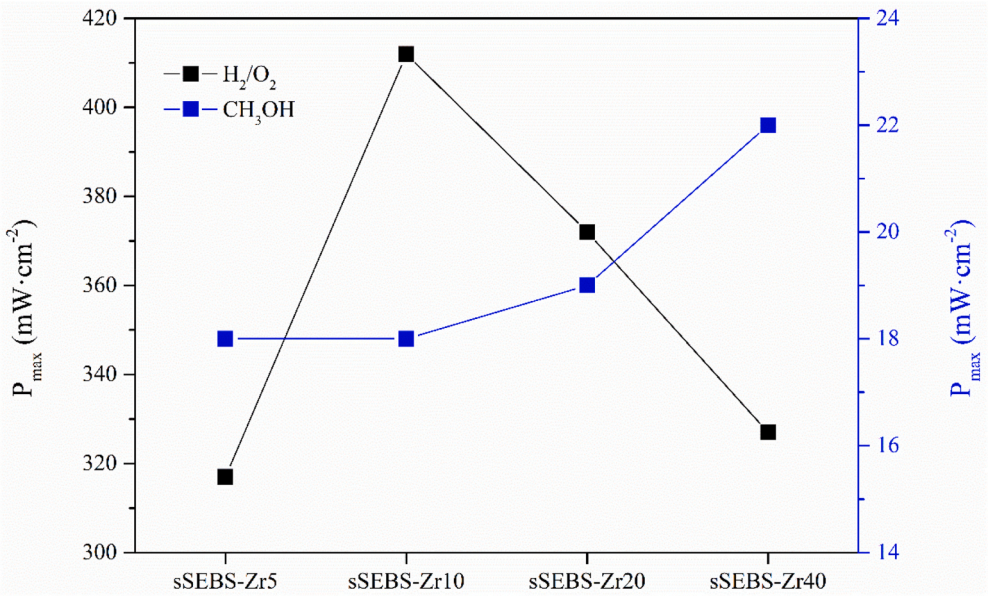

Fig. 9. Power density curves (100% relative humidity) of the hybrid sSEBS-Zr (sSEBS-Zr5, sSEBS-Zr10, sSEBS-Zr20 and sSEBS-Zr40) membranes measured at 333K.

values exhibited by Nafion 117 and other polymers measured at the same temperature, respectively [36,37,53–56].

Initially, through-plane proton conductivity analysis shows that sSEBS-Zr10 membrane has the higher proton conductive capacity at 333K in dry conditions. However, the best results in terms of power density is shown by sSEBS-Zr40 membrane, even though the excessive presence of inorganic component ($40SiO_2$–$40P_2O_5$–$20ZrO_2$) induce an excessive amount of M-O-M′ bonds with a consequent reduction of the available proton sites. As expected, these results ensure that proton conductivity is not the only determining factor on the behaviour of the cell. In fact, the ability of the hybrid membrane with the longest infiltration time to avoid crossover prevails over the proton transfer capability, contrary to what was detected in the hydrogen PEMFC. The phenomenon of methanol crossover causes significant voltage loss, waste of fuel and it is critical for the overall performance of the cell. Subsequently, sSEBS-Zr40 appears to be the most capable in DMFC among all hybrid membranes motivated by displaying the lowest electrical conductivity and enhanced chemical and mechanical resistance that decreases methanol crossover. Therefore, to validate any polymer for DMFC applications using the proposed methodology, a comprehensive analysis of the molecular motions and dielectric conductivity does not suffice. The crossover phenomena must be accounted to provide reliable results.

4. Conclusions

A series of hybrid sulfonated SEBS membranes have been characterized to further investigate their suitability for DMFC application. The addition of the inorganic component ($40SiO_2$–$40P_2O_5$–$20ZrO_2$) produces a plasticization effect reducing the glass transition temperature of the polystyrene block. Moreover, these hybrid membranes are more thermally stable than sSEBS, and this stability strengthens as the infiltration time increases.

The electric conductivity σ_{DC} obtained by dielectric thermal analysis reveals different behaviours of each hybrid membrane regarding the activated molecular motion. Regarding the α_{EB} zone, sSEBS, sSEBS-Zr10, and sSEBS-Zr20 display a nonlinear dependence concerning temperature, whereas sSEBS-Zr5 and sSEBS-Zr40 display a linear one. Therefore, there is a clear difference concerning the charge transfer mechanisms displayed by all membranes at this temperature region. Nonetheless, at higher temperatures, concerning the α_{PS} zone, all the membranes display the same nonlinear dependence, although the maximum peak is shifted towards higher temperature for the hybrid sSEBS-Zr membranes. The study of Jonscher's power law revealed no significant differences in the morphological texture of the hybrid membranes compared to sSEBS. Therefore, the segregated microstructure of sSEBS is maintained.

The proposed methodology where a comprehensive analysis of the molecular mobility and the charge transfer mechanisms is performed tailoring the membranes to be used as electrolytes in a Hydrogen PEM. Nevertheless, when these membranes are used as electrolytes in DMFCs, the previous analysis needs to be completed with other data accounting for the crossover phenomena because this can be other determining factor to obtain the maximum power density.

CRediT authorship contribution statement

B. Pascual-Jose: Formal analysis, Investigation, Writing – original draft, preparation. **C. del Río:** Conceptualization, Methodology, Investigation, Writing – review & editing, Resources, Supervision. **J. Mosa:** Methodology, Investigation. **A. Ribes-Greus:** Conceptualization, Methodology, Investigation, Resources, Writing – original draft, preparation, Writing – review & editing, Supervision, Funding acquisition.

Declaration of competing interest

The authors declare that they have no known competing financial interests or personal relationships that could have appeared to influence the work reported in this paper.

Data availability

The data that has been used is confidential.

Acknowledgments

The authors would like to thank the support of the European Union through the European Regional Development Funds (ERDF) and the Spanish Ministry of Economy, Industry, and Competitiveness for the research projects REPICOMES (ENE2017-90932-REDT) and POLYELMETH (PID2020-116322RB-C31).

References

[1] N. Tian, B.A. Lu, X.D. Yang, R. Huang, Y.X. Jiang, Z.Y. Zhou, S.G. Sun, Rational design and synthesis of low-temperature fuel cell electrocatalysts, Electrochem. Energy Rev. 1 (2018) 54–83, https://doi.org/10.1007/s41918-018-0004-1.

[2] M. Muthukumar, N. Rengarajan, B. Velliyangiri, M.A. Omprakas, C.B. Rohit, U. K. Raja, The development of fuel cell electric vehicles - a review, Mater. Today Proc. 45 (2021) 1181–1187, https://doi.org/10.1016/j.matpr.2020.03.679.

[3] S.D. Gaikwad, P.C. Ghosh, Sizing of a fuel cell electric vehicle: a pinch analysis-based approach, Int. J. Hydrogen Energy 45 (2020) 8985–8993, https://doi.org/10.1016/j.ijhydene.2020.01.116.

[4] M.A. Abdelkareem, K. Elsaid, T. Wilberforce, M. Kamil, E.T. Sayed, A. Olabi, Environmental aspects of fuel cells: a review, Sci. Total Environ. 752 (2021), 141803, https://doi.org/10.1016/j.scitotenv.2020.141803.

[5] A. Alaswad, A. Omran, J.R. Sodre, T. Wilberforce, G. Pignatelli, M. Dassisti, A. Baroutaji, A.G. Olabi, Technical and commercial challenges of proton-exchange membrane (Pem) fuel cells, Energies 14 (2021) 1–21, https://doi.org/10.3390/en14010144.

[6] Y. Wang, D.F. Ruiz Diaz, K.S. Chen, Z. Wang, X.C. Adroher, Materials, technological status, and fundamentals of PEM fuel cells – a review, Mater. Today 32 (2020) 178–203, https://doi.org/10.1016/j.mattod.2019.06.005.

[7] M.B. Karimi, F. Mohammadi, K. Hooshyari, Recent approaches to improve Nafion performance for fuel cell applications: a review, Int. J. Hydrogen Energy 44 (2019) 28919–28938, https://doi.org/10.1016/j.ijhydene.2019.09.096.

[8] C.Y. Wong, W.Y. Wong, K.S. Loh, W.R.W. Daud, K.L. Lim, M. Khalid, R. Walvekar, Development of poly(vinyl alcohol)-based polymers as proton exchange membranes and challenges in fuel cell application: a review, Polym. Rev. 60 (2020) 171–202, https://doi.org/10.1080/15583724.2019.1641514.

[9] I. Nicotera, C. Simari, A. Enotiadis, Nafion-based cation-exchange membranes for direct methanol fuel cells, in: Direct Methanol Fuel Cell Technol, INC, 2020, pp. 13–36, https://doi.org/10.1016/b978-0-12-819158-3.00002-1.

[10] M. Casciola, A. Donnadio, M. Pica, 3.7 basic aspects in proton-conducting membranes for fuel cells, in: Compr. Membr. Sci. Eng, Elsevier Ltd., 2017, pp. 171–205, https://doi.org/10.1016/b978-0-12-409547-2.12259-0.

[11] H. Junoh, J. Jaafar, N.A.H. Nik Abdul, A.F. Ismail, M.H.D. Othman, M.A. Rahman, F. Aziz, N. Yusof, Performance of polymer electrolyte membrane for direct methanol fuel cell application: perspective on morphological structure, Membranes (Basel) 10 (2020), https://doi.org/10.3390/membranes10030034.

[12] N. Awang, A.F. Ismail, J. Jaafar, T. Matsuura, H. Junoh, M.H.D. Othman, M. A. Rahman, Functionalization of polymeric materials as a high performance membrane for direct methanol fuel cell: a review, React. Funct. Polym. 86 (2015) 248–258, https://doi.org/10.1016/j.reactfunctpolym.2014.09.019.

[13] M.A. Abu-Saied, E.A. El-Desouky, E.A. Soliman, G.A. El-Naim, Novel sulphonated poly (vinyl chloride)/poly (2-acrylamido-2-methylpropane sulphonic acid) blends-based polyelectrolyte membranes for direct methanol fuel cells, Polym. Test. 89 (2020), 106604, https://doi.org/10.1016/j.polymertesting.2020.106604.

[14] H. Nagar, N. Sahu, V.V. Basava Rao, S. Sridhar, Surface modification of sulfonated polyethersulfone membrane with polyaniline nanoparticles for application in direct methanol fuel cell, Renew. Energy 146 (2020) 1262–1277, https://doi.org/10.1016/j.renene.2019.06.175.

[15] C.A. Edmondson, J.J. Fontanella, S.H. Chung, S.G. Greenbaum, G.E. Wnek, Complex impedance studies of S-SEBS block polymer proton-conducting membranes, Electrochim. Acta 46 (2001) 1623–1628, https://doi.org/10.1016/S0013-4686(00)00762-3.

[16] R. Teruel-Juanes, B. Pascual-Jose, C. del Río, O. García, A. Ribes-Greus, Dielectric analysis of photocrosslinked and post-sulfonated styrene-ethylene-butylene-styrene block copolymer based membranes, React. Funct. Polym. 155 (2020), 104715, https://doi.org/10.1016/j.reactfunctpolym.2020.104715.

[17] C. Del Río, O. García, E. Morales, P.G. Escribano, Single cell performance and electrochemical characterization of photocrosslinked and post-sulfonated SEBS-DVB membranes, Electrochim. Acta 176 (2015) 378–387, https://doi.org/10.1016/j.electacta.2015.07.009.

[18] H. Ahmad, S.K. Kamarudin, U.A. Hasran, W.R.W. Daud, A novel hybrid Nafion-PBI-ZP membrane for direct methanol fuel cells, Int. J. Hydrogen Energy 36 (2011) 14668–14677, https://doi.org/10.1016/j.ijhydene.2011.08.044.

[19] H. Ahmad, S.K. Kamarudin, U.A. Hasran, W.R.W. Daud, Overview of hybrid membranes for direct-methanol fuel-cell applications, Int. J. Hydrogen Energy 35 (2010) 2160–2175, https://doi.org/10.1016/j.ijhydene.2009.12.054.

[20] F. Bauer, M. Willert-Porada, Microstructural characterization of Zr-phosphate-Nafion® membranes for direct methanol fuel cell (DMFC) applications, J. Membr. Sci. 233 (2004) 141–149, https://doi.org/10.1016/j.memsci.2004.01.010.

[21] D. Dhanapal, M. Xiao, S. Wang, Y. Meng, A review on sulfonated polymer composite/organic-inorganic hybrid membranes to address methanol barrier issue for methanol fuel cells, Nanomaterials 9 (2019), https://doi.org/10.3390/nano9050668.

[22] Y. Huang, T. Cheng, X. Zhang, W. Zhang, X. Liu, Novel composite proton exchange membrane with long-range proton transfer channels constructed by synergistic effect between acid and base functionalized graphene oxide, Polymer 149 (2018) 305–315, https://doi.org/10.1016/j.polymer.2018.07.009.

[23] D.S. Kim, H.B. Park, J.W. Rhim, Y.M. Lee, Proton conductivity and methanol transport behavior of cross-linked PVA/PAA/silica hybrid membranes, Solid State Ionics 176 (2005) 117–126, https://doi.org/10.1016/j.ssi.2004.07.011.

[24] D.S. Kim, H.B. Park, J.W. Rhim, Y.M. Lee, Preparation and characterization of crosslinked PVA/SiO2 hybrid membranes containing sulfonic acid groups for direct methanol fuel cell applications, J. Membr. Sci. 240 (2004) 37–48, https://doi.org/10.1016/j.memsci.2004.04.010.

[25] H.K. Kim, H. Chang, Organic/inorganic hybrid membranes for direct methanol fuel cells, J. Membr. Sci. 288 (2007) 188–194, https://doi.org/10.1016/j.memsci.2006.11.038.

[26] O.V. Lebedeva, E.I. Sipkina, Y.N. Pozhidaev, Hybrid membranes based on silica and 2-hydroxyethylmethacrylate–4-vinylpyridine copolymers, Petrol. Chem. 56 (2016) 401–405, https://doi.org/10.1134/S0965544116050091.

[27] S. Meenakshi, A.K. Sahu, S.D. Bhat, P. Sridhar, S. Pitchumani, A.K. Shukla, Mesostructured-aluminosilicate-Nafion hybrid membranes for direct methanol fuel cells, Electrochim. Acta 89 (2013) 35–44, https://doi.org/10.1016/j.electacta.2012.11.003.

[28] A. Pagidi, M.M. Seepana, Synthesis of (Si-PWA)-PVA/PTFE high-temperature proton-conducting composite membrane for DMFC, Int. J. Hydrogen Energy 45 (2020) 25851–25861, https://doi.org/10.1016/j.ijhydene.2020.02.113.

[29] V. Parthiban, S. Akula, S.G. Peera, N. Islam, A.K. Sahu, Proton conducting nafion-sulfonated graphene hybrid membranes for direct methanol fuel cells with reduced methanol crossover, Energy Fuel. 30 (2016) 725–734, https://doi.org/10.1021/acs.energyfuels.5b02194.

[30] V. Parthiban, A.K. Sahu, Performance enhancement of direct methanol fuel cells using a methanol barrier boron nitride-Nafion hybrid membrane, New J. Chem. 44 (2020) 7338–7349, https://doi.org/10.1039/d0nj00433b.

[31] C. Ru, Y. Gu, H. Na, H. Li, C. Zhao, Preparation of a cross-linked sulfonated poly (arylene ether ketone) proton exchange membrane with enhanced proton conductivity and methanol resistance by introducing an ionic liquid-impregnated metal organic framework, ACS Appl. Mater. Interfaces 11 (2019) 31899–31908, https://doi.org/10.1021/acsami.9b09183.

[32] S. Shabanpanah, A. Omrani, M. Mansour Lakouraj, Fabrication and characterization of PVA/NNSA/GLA/nano-silica proton conducting composite membranes for DMFC applications, Des. Monomers Polym. 22 (2019) 130–139, https://doi.org/10.1080/15685551.2019.1626323.

[33] V. Vijayakumar, D. Khastgir, Hybrid composite membranes of chitosan/sulfonated polyaniline/silica as polymer electrolyte membrane for fuel cells, Carbohydr, Polym 179 (2018) 152–163, https://doi.org/10.1016/j.carbpol.2017.09.083.

[34] Y. Wang, D. Wang, J. Wang, L. Wang, Preparation and characterization of a sol-gel derived silica/PVA-Py hybrid anion exchange membranes for alkaline fuel cell application, J. Electroanal. Chem. 873 (2020), 114342, https://doi.org/10.1016/j.jelechem.2020.114342.

[35] Y.P. Ying, S.K. Kamarudin, M.S. Masdar, Silica-related membranes in fuel cell applications: an overview, Int. J. Hydrogen Energy 43 (2018) 16068–16084, https://doi.org/10.1016/j.ijhydene.2018.06.171.

[36] P.G. Escribano, C. del Río, E. Morales, M. Aparicio, J. Mosa, Infiltration of 40SiO2−40P2O5−20ZrO2 sol-gel in sSEBS membranes for PEMFCs application, J. Membr. Sci. 551 (2018) 136–144, https://doi.org/10.1016/j.memsci.2018.01.044.

[37] O. Santiago, J. Mosa, P.G. Escribano, E. Navarro, E. Chinarro, M. Aparicio, T.J. Leo, C. del Río, 40SiO2–40P2O5–20ZrO2 sol-gel infiltrated sSEBS membranes with improved methanol crossover and cell performance for direct methanol fuel cell applications, Int. J. Hydrogen Energy 45 (2020) 20620–20631, https://doi.org/10.1016/j.ijhydene.2020.01.252.

[38] J.R. MacDonald, Comparison of the universal dynamic response power-law fitting model for conducting systems with superior alternative models, Solid State Ionics 133 (2000) 79–97, https://doi.org/10.1016/S0167-2738(00)00737-2.

[39] X. Qian, N. Gu, Z. Cheng, X. Yang, E. Wang, S. Dong, Methods to study the ionic conductivity of polymeric electrolytes using a.c. impedance spectroscopy, J. Solid State Electrochem. 6 (2001) 8–15, https://doi.org/10.1007/s100080000190.

[40] F. Müller, C.A. Ferreira, L. Franco, J. Puiggalí, C. Alemán, E. Armelin, New sulfonated polystyrene and styrene–ethylene/butylene–styrene block copolymers for applications in electrodialysis, J. Phys. Chem. B 116 (2012) 11767–11779.

[41] A. Ganguly, A.K. Bhowmick, Sulfonated styrene-(ethylene-co-butylene)-styrene/montmorillonite clay nanocomposites: synthesis, morphology, and properties, Nanoscale Res. Lett. 3 (2008) 36–44, https://doi.org/10.1007/s11671-007-9111-3.

[42] M.K. Mistry, N.R. Choudhury, N.K. Dutta, R. Knott, Inorganic modification of block copolymer for medium temperature proton exchange membrane application, J. Membr. Sci. 351 (2010) 168–177, https://doi.org/10.1016/j.memsci.2010.01.044.

[43] N.S. Karode, A. Poudel, L. Fitzhenry, S. Matthews, P.R. Walsh, A.B. Coffey, Evaluation of interfacial region of microphase-separated SEBS using modulated differential scanning calorimetry and dynamic mechanical thermal analysis, Polym. Test. 62 (2017) 268–277, https://doi.org/10.1016/j.polymertesting.2017.07.006.

[44] W.J. Lee, H.R. Jung, M.S. Lee, J.H. Kim, K.S. Yang, Preparation and ionic conductivity of sulfonated-SEBS/SiO 2/plasticizer composite polymer electrolyte for polymer battery, Solid State Ionics 164 (2003) 65–72, https://doi.org/10.1016/S0167-2738(03)00298-4.

[45] M. Yan, Y. Lu, N. Li, F. Zeng, Q. Wang, H. Bai, Z. Xie, Hyperbranch-crosslinked S-SEBS block copolymer membranes for desalination by pervaporation, Membranes (Basel) 10 (2020) 1–16, https://doi.org/10.3390/membranes10100277.

[46] K.A. Mauritz, R.I. Blackwell, F.L. Beyer, Viscoelastic properties and morphology of sulfonated poly(styrene-b- ethylene/butylene-b-styrene) block copolymers (sBCP), and sBCP/[silicate] nanostructured materials, Polymer 45 (2004) 3001–3016, https://doi.org/10.1016/j.polymer.2003.12.078.

[47] H. Chen, M.K. Hassan, S.K. Peddini, K.A. Mauritz, Macromolecular dynamics of sulfonated poly (styrene-b-ethylene-ran-butylene-b-styrene) block copolymers by broadband dielectric spectroscopy, Eur. Polym. J. 47 (2011) 1936–1948, https://doi.org/10.1016/j.eurpolymj.2011.07.005.

[48] V. Bocharova, A.P. Sokolov, Perspectives for polymer electrolytes: a view from fundamentals of ionic conductivity, Macromolecules 53 (2020) 4141–4157, https://doi.org/10.1021/acs.macromol.9b02742.
[49] C. Gainaru, E.W. Stacy, V. Bocharova, M. Gobet, A.P. Holt, T. Saito, S. Greenbaum, A.P. Sokolov, Mechanism of conductivity relaxation in liquid and polymeric electrolytes: direct link between conductivity and diffusivity, J. Phys. Chem. B 120 (2016) 11074–11083, https://doi.org/10.1021/acs.jpcb.6b08567.
[50] A. Kisliuk, V. Bocharova, I. Popov, C. Gainaru, A.P. Sokolov, Fundamental parameters governing ion conductivity in polymer electrolytes, Electrochim. Acta 299 (2019) 191–196, https://doi.org/10.1016/j.electacta.2018.12.143.
[51] P. Singh, P.N. Gupta, A.L. Saroj, Ion dynamics and dielectric relaxation behavior of PVA-PVP-NaI-SiO2 based nano-composites polymer blend electrolytes, Phys. B Condens. Matter 578 (2020), 411850, https://doi.org/10.1016/j.physb.2019.411850.
[52] K.A. Mauritz, Dielectric relaxation studies of ion motions in electrolyte-containing perfluorosulfonate ionomers. 4. Long-range ion transport, Macromolecules 22 (1989) 4483–4488.
[53] R.I. Blackwell, K.A. Mauritz, Nanostructured organic/inorganic materials based on sol-gel processes in sulfonated poly [styrene-Co-(Ethylene-Butylene)-Co-styrene] (SEBS) block copolymers, Polym. Prepr. (Am. Chem. Soc., Div. Polym. Chem.) 43 (2002) 1341–1342.
[54] F. Lufrano, V. Baglio, P. Staiti, V. Antonucci, Performance analysis of polymer electrolyte membranes for direct methanol fuel cells, J. Power Sources 243 (2013) 519–534.
[55] A. Sivasankaran, D. Sangeetha, Y.H. Ahn, Nanocomposite membranes based on sulfonated polystyrene ethylene butylene polystyrene (SSEBS) and sulfonated SiO2 for microbial fuel cell application, Chem. Eng. J. 289 (2016) 442–451, https://doi.org/10.1016/j.cej.2015.12.095.
[56] D.H. Jung, Y.-B. Myoung, S.-Y. Cho, D.R. Shin, D.H. Peck, A performance evaluation of direct methanol fuel cell using impregnated tetraethyl-orthosilicate in cross-linked polymer membrane, Int. J. Hydrogen Energy 26 (2001) 1263–1269.